Solar flare-induced gradient drift instability observed by SuperDARN HF radars

S. Chakraborty[1], N. Nishitani[2], X. Shi[3,4], P. Ponomarenko[5], J. M. Ruohoniemi[3], J. B. H. Baker[3], A. J. Coster[6], I. Häggström[7]

[1]Embry-Riddle Aeronautical University, Daytona Beach, FL, USA
[2]Institute for Space-Earth Environmental Research, Nagoya University, Aichi, Japan
[3]Department of Electrical and Computer Engineering, Virginia Tech, Blacksburg, VA, USA
[4]High Altitude Observatory, NCAR, Boulder, CO, USA
[5]University of Saskatchewan, Saskatoon, Canada
[6]Haystack Observatory, Massachusetts Institute of Technology, Westford, MA
[7]European Incoherent Scatter Scientific Association (EISCAT), Kiruna, SE-981 92, Sweden

Key Points:

- A sudden appearance of SuperDARN ionospheric scatters (IS) following an X9.3 class flare near the dawn terminator
- IS are most likely formed by Gradient Drift Instability due to the flare-enhanced density gradient
- Intense Doppler velocity in the observed IS indicates a stronger localized electric field

Corresponding author: Shibaji Chakraborty, chakras4@erau.edu

Abstract

Solar flares, are rapid increase in solar irradiance specifically in X-ray and Extreme Ultra Violet spectra, enhance the ionization in the dayside ionosphere and create Sudden Ionospheric Disturbances (SIDs). SIDs are known to create space weather impacts on the traveling high frequency (HF:3-30 MHz) radio wave, by disrupting the communication channels. In this study, we examine a less-known geophysical phenomena that stems from a severe X9.3 flare, utilizing SuperDARN HF coherent scatter radars and Global Navigation Satellite System (GNSS) Total Electron Content (TEC) observations. Specifically, we are interested in the transients in the ionospheric electrodynamics at the sub-auroral latitude near the terminator stem from the flare effect. Observations suggest that flare-induced density gradient likely favor the formation of gradient-drift instability near the dawn terminator, leading to the irregularities observed by the SuperDARN radars with line-of-sight (LoS) Doppler velocity reaching nearly 300 m/s. The flare amplifies the eastward TEC gradient near the dawn terminator by approximately 2-3 times compared to a geomagnetically quiet day. Observations suggest that flare-induced density gradients likely favor the formation of Gradient-Drift Instability near the dawn terminator, leading to the irregularities observed by the SuperDARN radars. In contrast to prior study indicating decreased cross polar-cap potential and associated ionospheric convection flow, our findings show the flare is followed by an increase in localized electric field near the dawn terminator as depicted in radar LoS velocity.

Plain Language Summary

Solar flares cause disturbances in the upper atmosphere, particularly in the layer containing charged particles called the ionosphere. These disturbances result in sudden changes in the Total Electron Content (TEC) of the ionosphere during daytime. Previous research has demonstrated that these disturbances affect the propagation of radio waves by increasing absorption of high-frequency signals and changing the path lengths they travel. Our study focuses on a previously unexplored aspect of these disturbances caused by solar flares. We have observed a transient phenomenon occurring in the radio waves traveling through the ionosphere during flare events. We aim to understand the cause and mechanism behind this phenomenon, which involves instability processes in the plasma present in the ionosphere. Through this study, we seek to shed light on how these flare-driven plasma instability processes occur and their implications. We used SuperDARN radar observations along with GNSS TEC dataset to understand the flare-driven sub-auroral latitude ionospheric electrodynamics.

1 Introduction

A solar flare is a sudden brightening of solar disk, specifically in X-rays and Extreme Ultra Violet (EUVs) spectrum. Solar flares are known to create strong perturbations in the dayside ionosphere by enhancing the photoionization, commonly refereed to as Sudden Ionospheric Disturbances (SIDs). SID is a space weather condition that create transients in the dayside ionosphere, specifically disrupts radio communication channels including Very Low Frequency (VLF: 3-30 kHz) (e.g., Belcher et al., 2021, & references therein), High Frequencies, (HF: 3-30 MHz) (e.g., Chakraborty et al., 2018, 2019), and satellite communications (e.g., Cheng et al., 2019). The flare-driven impact can also induce transients in ionospheric current systems which in turn create disturbances in geomagnetic fields recorded by the ground magnetometers (e.g., Curto et al., 2018; Manju & Viswanathan, 2005; Dodson & Hedeman, 1958). Large flares can severely impact high-latitude ionospheric electrodynamics and may create detectable signatures in Earth's magnetosphere via magnetosphere-ionosphere (MI) coupling (Liu et al., 2021). However, there are only a few observational studies that have delved into this flare-driven changes in the MI coupling processes (e.g., Sergeyev, 1977; Yamauchi et al., 2020).

Coherent scatter Doppler radars known to observe scatters from F-region altitudes near the dusk terminator (Ruohoniemi et al., 1988), commonly refereed to as Dusk Scatter Event (DUSE). Later Hosokawa and Nishitani (2010) conducted a statistical study using coherent HF radars located in the high (auroral) and middle latitudes, and reported DUSE are a recurring phenomena. Additionally, the study reported similar phenomena observed near the dawn terminator, and commonly refereed to as Dawn Scatter Event. Hosokawa and Nishitani (2010) employed SuperDARN HF radar observations to statistically demonstrate that even on geomagnetically quiet days F-region irregularities can arise near the day-night terminator through the Gradient-Drift Instability (GDI), facilitated by the density gradients near the terminators (e.g., Tsunoda, 1988).

Gradient Drift Instability (GDI) is an interchange of two elements of fluid plasma or the same element with different densities separated by a sharp gradient (Tsunoda, 1988). It can be categorized as a modified Rayleigh-Taylor instability (Kelley, 2009). Due to external forcing, if a density gradient is present in a magnetized plasma and a slight disturbance occurs, charge separation can take place which produces a small localized 'Polarization Electric Field'. The polarization electric field feeds the disturbance and charges separation in the presence of a magnetic field, thus producing instability. SuperDARN measured irregularities are often observed near terminators, primarily at sub-auroral latitudes (Hosokawa et al., 2000; Tsunoda, 1988). Hosokawa et al. (2000) showed that solar flare can also trigger ionospheric irregularities near the day-night terminators, particularly at sub-auroral latitudes, specifically near the equatorial boundary of the auroral oval. However, there are not many studies that have reported and explained the mechanism of such events.

Extreme solar flares can increases the likelihood of GDI-generated F-region irregularities by amplifying plasma density gradients near the terminator. (Hosokawa et al., 2000) noted these irregularities emerging at auroral latitudes, especially at the equatorward boundary of convection return flow. Furthermore, their study uncovered distinct magnetometer responses on the poleward and equatorward sides of the irregularity structure. Notably, magnetometers located toward the poleward side exhibited prolonged and more pronounced deviations in horizontal geomagnetic components following the flare. Other prior studies (e.g., Yamazaki & Maute, 2017; Yamauchi et al., 2020) speculated that variances in magnetometer responses across latitudes may stem from the electric field or conductivity structure discontinuities. However, the studies did not provide any quantification against the GDI growth rates.

This study presents less known ionospheric phenomena captured by HF radars located at high latitudes following a massive X9.3-class flare that occurred on September 6, 2017 that peaked at 12:02 UT. A novel data analysis approach utilizing a horizontal Total Electron Content (TEC) gradient, alongside line-of-sight (LoS) Doppler velocity from SuperDARN radars, is employed to compute a growth rate proxy of the instability, which is considered to be GDI. Notably, our findings include: (1) the sudden appearance of field-aligned irregular structures in the high-latitude dawn sector aligned with the ionospheric convection return flow with a peak LoS velocity ~ 300 m/s; and (2) a 3-4 times amplification in the instability growth rate proxy as compared to low geophysical activity days. Moreover, we ascertain that the commencement of GDI in the high-latitude region is predominantly triggered by the enhanced horizontal gradient (as indicated by the TEC data) and the enhanced ionospheric electric field (as indicated by the SuperDARN LOS velocity measurements).

2 Datasets and Methodology

2.1 GDI Formation Mechanism

Near the sub-auroral latitude dawn terminator at the F region heights, we observe a sharp plasma density gradient from night to the dayside. Being a dayside phenomenon solar flares significantly increase the density gradient compare to a geophysically quiet day, which leads to a suitable scenario to stem GDI. GDI formation mechanism is primarily dependent on the geometry of the density gradient of two fluids, background electric, magnetic fields, and plasma flow direction, which are different in the F-region altitudes. Note that near the dawn/dusk terminator, the F-region is not well-formed at the nightside, compared to the dayside. Thus, we use F-region to refer to altitudes where electrons/ions are both collisionless (≥150 km).

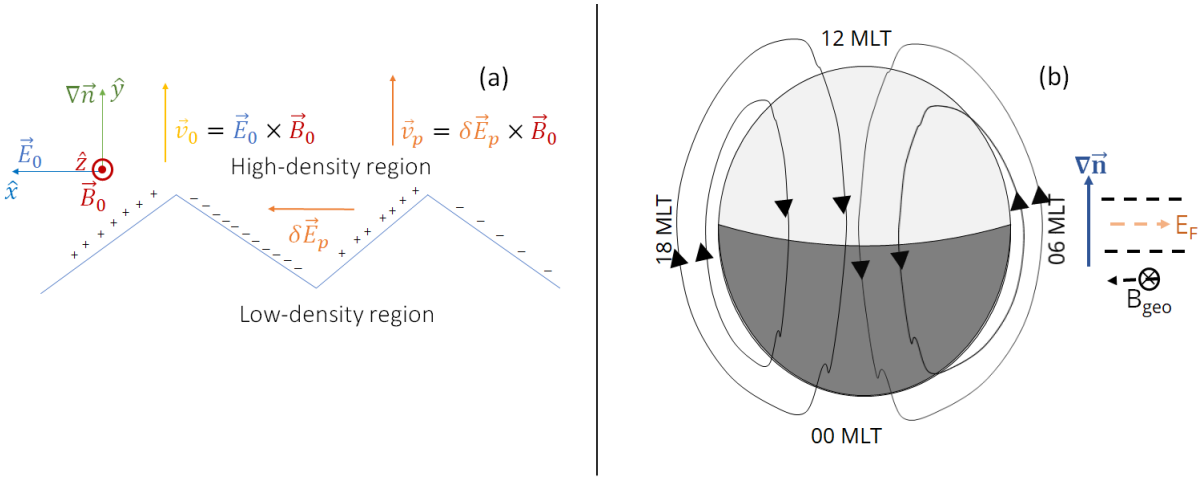

Figure 1. Schematic showing formation of GDI in a flare-modified ionosphere near the dawn terminator: (a) formation mechanism of GDI in F-region ionosphere and directions of background parameters ($\vec{E}_0$,$\vec{B}_0$,$\nabla\vec{n}$), Hall drift velocity ($\vec{v}_0$), polarization E-field (δE_p), and Hall drift under polarization E-field ($\vec{v}_p$); (b) GDI formation and geometry of the background parameters near dawn side terminator (06 MLT). Parameters and associated directions in panel (a) are color-coded.

Figure 1 puts the geometry of the GDI formation mechanism in the context of the dawn side F-region ionosphere. The ambient electric field at F-region height is projected from the magnetosphere and near the dawn side ionosphere is along the x-axis (it is equatorward directed or north-to-south). The ambient magnetic field is out of the page, along the z-axis (at the high latitude it is northward directed and tilted towards the ground). At F-region altitude both ions and electrons are collisionless. The charge separation at F-region altitude is produced through the large Pedersen mobility of the ions as compared to that of electrons. The Pedersen mobility ion (due to their heavy weights) causes a charge separation that leads to polarization electric field along the x-axis (along the terminator) which can grow into instability.

The strength of the background parameters plays a significant role in determining if the instability will form or not. Flare will certainly enhance the west-east gradient near the terminator (refer to Figures 1), which makes it more favorable for GDI formation. In this study we provide empirical evidence that the GDI is the formation mechanism of the sudden appearance of IS observed at the high latitude radars. We can use the GDI growth rate to quantify the chance of GDI occurrence relative to a geophysically quiet

day and validate if it is the primary source of the IS observed by the SuperDARN radars. The GDI growth rate [first-order approximation] can mathematically be described below [equation (1) (Tsunoda, 1988)]

$$\gamma = \frac{V_0}{n_0}\frac{\partial n_0}{\partial \phi} \tag{1}$$

where, γ, V_0, n_0, and ϕ are GDI growth rate, plasma flow velocity, background electron density at F-region altitude, and longitude, respectively. Hence, $\frac{\partial n_0}{\partial \phi}$ represents the gradient of n_0 along longitude [a horizontal component of electron density gradient along east-west].

We know that the GDI growth rates get impacted by the diffusion near the diffusive subranges (wave number ranges where diffusion dominates and impedes growth of the instability) (e.g., Kelley, 2009). In this study we used the most simplified form of the liner GDI growth rate 1. However, at diffusive subranges, we can expect plasma diffusion (parallel and ambipolar) that leads to dissipation of the GDI spawn waves, specifically smaller wave number (k), and the equation becomes $\gamma = \frac{V_0}{n_0}\frac{\partial n_0}{\partial \phi} - k^2 D_\perp$, where k and $D_\perp$ are the wave number and diffusion constant. This term suggests that while a gradient tries to spawn instability the small-scale wave structures can be damped by the diffusion process. Instability stems from GDI with a large wavelength (small wave number k) less susceptible to diffusion and leads to efficient instability growth. Following Kelley (2009), we find a reasonable non-diffusive F-region critical wavelength is 3-meters, suggesting any instability wave stem by GDI above 3-meters would not be dissipate through diffusion. Given SuperDARN observes decameter scale irregularities (30 meter wavelength range), above the critical wavelength at F-region, hence the observed structures using SuperDARN is physical and can be backed by the above theory.

2.2 Super Dual Auroral Radar Network

Super Dual Auroral Radar Network, SuperDARN, is an international collaboration of HF radar network that spans the middle, high, and polar latitudes of both hemispheres (Greenwald et al., 1985; Chisham et al., 2007; Nishitani et al., 2019). The system employs 16-24 azimuthal beams covering 75-110 range gates spaced by 45 km starting from the 180 km group range. A 3-s or 6-s integration time per beam results in a full radar sweep within 1-2 minutes. Prior studies have utilized ground scatter (GS) SuperDARN echoes for characterizing flare impact observed by HF communication channels (Watanabe & Nishitani, 2013; Chakraborty et al., 2018), whereas this study employs ionospheric scatter (IS) to detect flare-driven ionospheric electrodynamics transients. This investigation focuses on SuperDARN radar fields-of-view (FoV) distributed across the Northern American sector (Figure 2(a)). The radars shown in Figure 2(a) probe high/auroral latitudes, with beam 7 of Saskatoon and Prince George and beam 10 of Kodiak radars highlighted in blue. The gray-shaded area signifies the nightside of Earth at F-region altitudes (300 km) during the peak of the X9.3 class flare on 6 September 2017, at 12:02 UT. The red shaded area indicates a $3^\circ \times 3^\circ$ region that is used to calculate a horizontal TEC gradient, investigate the source of IS observed by the radars, and numerically quantify the effects following the solar flare.

2.3 GNSS TEC

In this research, Global Navigation Satellite System (GNSS) Total Electron Content (TEC) data play a pivotal role (David & Sojka, 2019). TEC data serve as a proxy for the peak electron density (Nishioka et al., 2021). To show the electron density gradient at F-region altitudes along latitude and longitude, we utilized the horizontal gradient of TEC [$\nabla_{(\lambda,\phi)}$TEC, where λ denotes latitude and ϕ denotes longitude] (Jakowski & Hoque, 2019). Our analysis involves utilizing vertical TEC observations from the MIT Haystack Madrigal database, sourced from various stations situated across the North American sector (Coster et al., 2017). For this study we are going to use the horizontal gra-

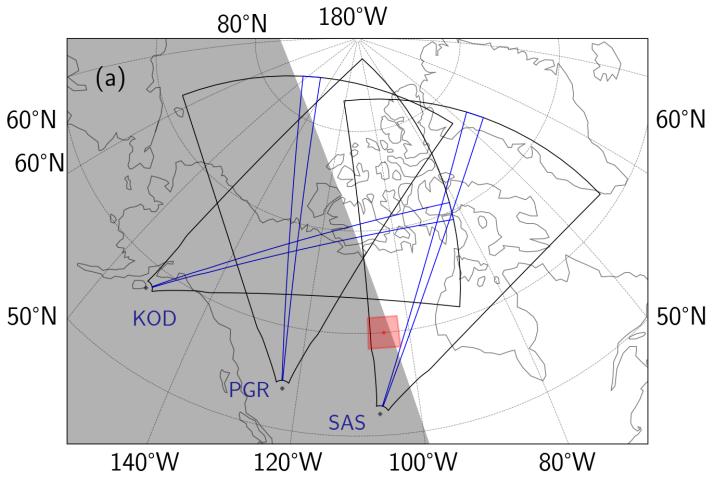

Figure 2. Fields-of-View of the SuperDARN high latitude radars used in this study. The radars are Saskatoon [SAS], Prince George [PGR], and Kodiak [KOD]. The regions enclosed by the blue lines indicate beam 7 for SAS and PGR and beam 10 for KOD radar, respectively. The nightside at F-region heights is indicated by grey shading. The red-shaded region indicates a $3^\circ \times 3^\circ$ cell ($\lambda, \phi = 60^\circ, -105^\circ$) used to investigate the source of IS observed by the radar and numerically quantify the effects (see text for details).

dient of TEC as a proxy of NmF_2 and to quantify growth rate of GDI. While the time derivative of the TEC has been used to show the temporal variations of various geophysical phenomena (Amaechi et al., 2021), the spatial gradient in TEC observations can be very useful to identify and analyze large-scale spatial structures like sub-auroral ionospheric trough (Nishimura et al., 2021), traveling ionospheric disturbances (Belehaki et al., 2020), tongue of ionization (Klimenko et al., 2019) etc.

2.3.1 Estimating horizontal gradient of TEC

To show the electron density gradient along latitude and longitude:

$$\nabla_{(\lambda,\phi)} = \frac{\partial^2 TEC}{\partial\lambda\partial\phi} \tag{2}$$

In a study, conducted by Jakowski and Hoque (2019), a novel approach was introduced for the calculation of horizontal components of TEC gradient using slant TEC data. This innovative method involved selecting specific TEC components based on their associated elevation angles, a technique essential for obtaining accurate horizontal information from the TEC measurements. Moreover, the study revealed a significant correlation between density gradients in the ionosphere and the occurrence of solar flare-induced SIDs. We employ the similar technique described in the literature to compute spatial gradient in TEC.

Figure 3 presents the longitudinal (east-west component of the horizontal) gradient ($\frac{\partial}{\partial\phi}$TEC) from vTEC obtained from Madrigal Website, which provides $1^\circ\times1^\circ$ latitude-longitude girded vTEC data in 5-minute cadence in gray shading. Figure also presents gradients computed on $3^\circ\times3^\circ$ latitude-longitude grids, as shown by the black quivers. The day-night terminator is overlaid on top of the map at 11:47 UT. From this analysis. Note that, we binned $1^\circ \times 1^\circ$ latitude/longitude gridded TEC into a $3^\circ \times 3^\circ$ lati-

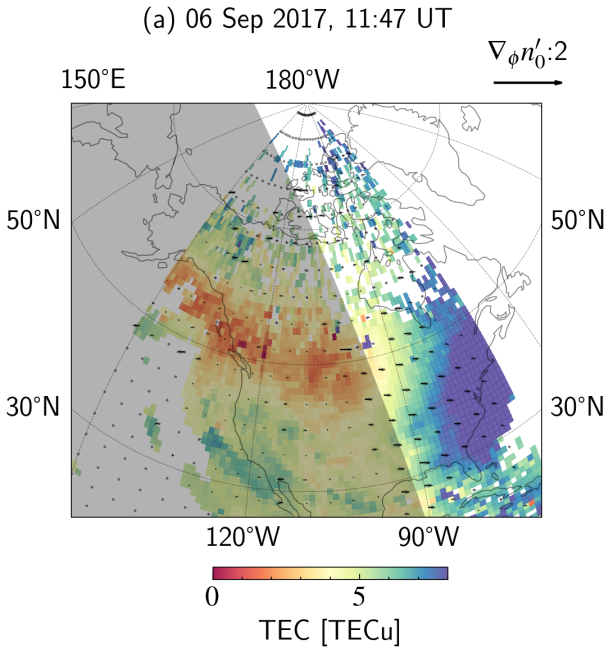

Figure 3. Example plots describing the methodology of extracting horizontal TEC gradients from the Madrigal Website, girded into $3° \times 3°$ latitude-longitude grid.

tude/longitude bin to calculate the horizontal gradient and reduce noises in the estimated gradient. We tested $1° \times 1°$, $2° \times 2°$, and $3° \times 3°$ grids to calculate TEC gradient and find that a $3° \times 3°$ latitude-longitude gridded observation reduces the noise and organizes the gradient as expected near the terminator (please refer to supplementary document).

The precision of the TEC measurement comes from various sources including measurement of carrier phase data, calculation, binning the data into latitude/longitude grids, number of receivers in a bin, elevation angle etc. We used $1° \times 1°$ latitude/longitude TEC grid dataset for this analysis from MIT Madrigal database. By checking the values of errors listed in the TEC files we confirm that most of the errors in TEC measurement are less than 0.3 TECu, which is <7% relative error in the observations, suggesting the datasets can be used to estimate TEC gradient.

2.4 ISR Tromsø Observations

While solar flares increase ionization on the total dayside ionosphere, the impact is not proportional in all ionospheric regions (e.g., Huang et al., 2014; Qian et al., 2010; Chamberlin et al., 2020). The data presented in Figure 4 is electron density observation from EISCAT Tromsø ISR VHF (224 MHz) radar located at 69^o geographic latitudes, looking northward at its lowest elevation angle (30^o) above the horizon towards the geographic North (360^o) azimuth. The top panels show the electron density as a function of altitude and time showing a rapid enhancement of photoionization near the solar flare peak indicated by the vertical black line. We can see a significant density enhancement in all ionospheric regions. Analysis of the electron density at different altitudes (shown in the middle panel) provides a deeper understanding of the electron density profile following the solar flare. The ratio of electron density during the peak of the flare to the background (indicated by θ_{N_e}) and absolute change to the background (indicated by δ_{N_e}) is also listed on the panel. We see a significant change in electron density at around 100

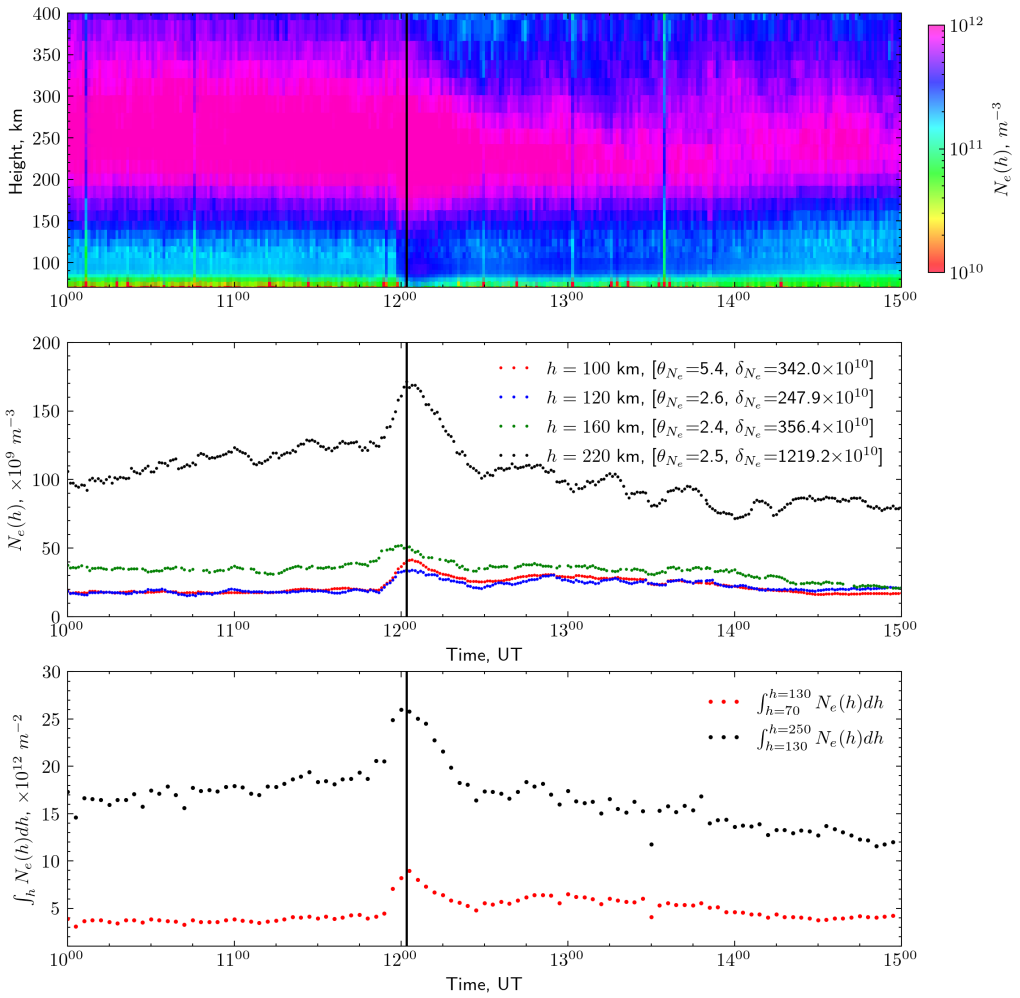

Figure 4. Ionospheric line-of-sight electron density observations from EISCAT Tromsø VHF (224 MHz) radar, located at 69° gegraphic latitude position looking geographic northward (azimuth angle = 0°) at its lowest elevation angle (30°). From top to bottom panels present time series of: (a) electron density profile, (b) electron density at specific heights (100, 120, 160, and 220 km altitudes in red, blue, green, and black), and (c) height integrated electron density from 70-130 km altitudes (in red) and 130-250 km altitudes. The vertical black line in all panels represents the peak of the X9.3 class solar flare.

km altitude. The change drops around 120 km, increases around 150 km, and peaks around 220 km. Finally, the bottom panel shows the integrated electron density for the D and E regions (between 70-130 km in red) and the F-region (between 130 and 250 km, in blue), respectively. This data set represents the total amount of energy deposition as a function of ionospheric region/altitude followed by the flare and associated change in TEC observations. While the percentage change in D/E-regions together is about 240% than background the same for F-region is around 160%. In contrast absolute electron content change at F-region altitude is 12.9×10^{12} m^{-2}, which is much larger than the same in D and E-regions together 4.6×10^{12} m^{-2}. Analysis suggests that while we can expect the percentage change to be highest at lower ionospheric altitudes the absolute change is much higher at the F-region altitudes, and these findings are consistent with the previous studies (e.g., Chakraborty et al., 2021, and references there in). The F-region is determined to be responsible for 73.7% of the total increase in TEC, with the remainder originating from the bottomside ionosphere.

3 Observations

This section introduces the event by showing the interplanetary magnetic field (IMF), solar wind, and othe geophysical conditions including solar irradiance, geomagnetic indices, and ionospheric response from the Saskatoon (SAS) SuperDARN radar. On September 6, 2017, an extreme X9.3 class flare erupted from solar active region AR 12673, marking the most intense flare of the last solar cycle (2008-2019). Its onset and peak occurred at 11:56 and 12:02 UT, respectively. Figure 5(a-e) presents the geophysical conditions and Saskatoon radar response, encompassing: (a) solar X-ray irradiance from GOES-15 satellite X-ray sensor with two channels 0.1-0.8 nm and 0.05-0.4 nm, (b) interplanetary magnetic fields, (c) solar wind velocity (in magenta), proton density (in black) and dynamic pressure (in blue), (d) ASYM-H/SYM-H indices depicting ring current responses, (e) auroral indices characterizing auroral electrojets (AE, AL, and AU), and (f) a range-time intensity (RTI) plot showcasing Line-of-Sight (LoS) Doppler velocity recorded along beam 7 of the SuperDARN Saskatoon radar. Note that another X-class (X1.2) flare preceding this event, with the subsolar point over Central Europe, had no impact on SuperDARN radars over North America which were on the nightside at that moment. However, it elevated the background electron density as compared to a typical quiet day. The solar irradiance following the X9.3 class flare remained elevated for approximately 12 hours, which caused wide-scale HF disruption (e.g., Chakraborty et al., 2019; Frissell et al., 2019). After the flare, other smaller X- and multiple M-class flares emerged during its decay phase. Both IMF $B_{(y,z)}$ ranged between (-2 nT, -4 nT), which is indicative of a polar ionosphere with a nearly symmetrical two-cell convection pattern. Solar wind parameters suggest that there was a relatively small sudden enhancement in solar wind proton density and dynamic pressure around 8 UT. AE and AL indices showed heightened values from around 8 UT, and AE and AU indices exhibited transient enhancements. Yamauchi et al. (2020) showed an enhancement in the auroral current system was triggered by the solar flare. Additionally, we observed a transient enhancement in the partial ring current system [ASYM-H, panel (d) blue curve], signifying modifications in the dayside middle and low latitude current structures. Finally, we see the sudden appearance of high-velocity ionospheric scatter (red patch after the vertical red line) in the SuperDARN Saskatoon radar observations following the solar flare (indicated by the vertical black line), which lasted for approximately 3 hours.

For comparison, we choose 30th August 2017 as a geomagnetically quiet day, which only experienced a single M-class flare later in the Universal Time (UT) day. Interestingly, the IMF observations for both days show no substantial differences, with the IMF fluctuating around 0 nT on both occasions. Quiet day selection criteria fit many days in August 2017, but we are also interested in a day where SAS radar observed ionospheric

data near the dawn terminator, so that we can estimate growth rate proxy and compare between quiet and event days.

We did a virtual height and spectral (decay rate) analysis of the backscatter echoes observed by the SAS radar (blob that appeared between 1000-2000 km after the flare peak 12:02 UT and near the day-night terminator) to confirm its possible altitude location and sources. The virtual height models suggested that the backscatter echoes were most likely coming between virtual heights of 350-650 km (Chisham et al., 2007). Additionally, the spectral analysis shows a higher decay rate of the backscatter echo population suggesting the echoes were ionospheric. Consequently, this analysis suggests that these are ionospheric backscatter from 150 km and above. We analyzed the dataset from all the radars used in this study, and they agreed with this conclusion. We have added the figures in the supplementary document to support this claim and for the readers. Additionally, from previous studies, we understand these dawn/dusk scatters appearing near the terminators are F-region ionospheric scatter (Hosokawa & Nishitani, 2010).

SuperDARN radars strategically positioned across the North American sector, as depicted in Figure 2, captured the sudden emergence of ionospheric irregularity backscatters, occurring from minutes to hours after the peak of the flare. Figure 6 presents RTI plots of LoS Doppler velocity from SuperDARN radars probing auroral latitudes, spanning the period from 11 to 17 UT on September 6, 2017. Panels (a-c) feature observations from beam 7 of radars Saskatoon (SAS), Prince George (PGR), and beam 10 of Kodiak (KOD), respectively. The vertical black line corresponds to the flare peak, while the gray-shaded region signifies the zone with a solar zenith angle greater than 90° at F-region altitude ($\sim$ 300 km), indicating the nightside. The radars observed the phenomena about 3, 3 hours 25 minutes and 2 hours 30 minutes, respectively. Note the sudden emergence of high-velocity ionospheric scatter (IS) near the day-night terminator for all three radars. Key observations include: (1) the abrupt emergence of field-aligned irregularity formations (red or blue color-coded high-velocity IS) immediately after the dawn terminator; (2) longer duration and stronger intensity of LoS Doppler velocity linked with flare-induced IS compared to a quiet day; (3) although the flare peaked at 12:02 UT, radars in the pre-dawn sector only recorded the field-aligned irregularities once their beams (or Fields-of-View) transitioned into the sunlit sector (near to the dawn terminator). The feature is not moving or co-rotating, rather radars are co-rotating with the Earth and as their fields-of-view reach near the terminator, they start recording the observations.

To investigate the source of these IS echoes, Figure 7 presents a map of the east-west horizontal gradient of TEC for the event date (6 September on the left column [a-b]) and compares it with a geophysically quiet day (30 August on the right column [c-d]) at the same UT time. We compared the observations between the selected days before the event time (top row [a,c]) and after the event time (bottom row [b,d]). Key observations encompass: (1) the sudden appearance of high velocity IS following the flare on the flare day, while the IS already existed on the quiet day; (2) the spatial extent and velocity of the IS that appeared on the flare day are significantly larger and stronger than that during the quiet day. Note that not all quiet days show IS near the dawn terminator. These findings argue that the sudden appearance of high-velocity IS on Sep 6, 2017 is related to the solar flare occurring at the same time.

4 Discussion

Ionospheric F-region irregularities arise from plasma density fluctuations that undergo amplification through diverse plasma instability processes (Fejer & Kelley, 1980; Keskinen & Ossakow, 1983; Tsunoda, 1988). The emergence of GDI near the dawnside F-region ionosphere hinges upon the specifics of E-field and B-field geometry, coupled with plasma flow direction, and the magnitudes of these parameters (Tsunoda, 1988). Near the dawn terminator, the plasma density gradient is oriented primarily from west

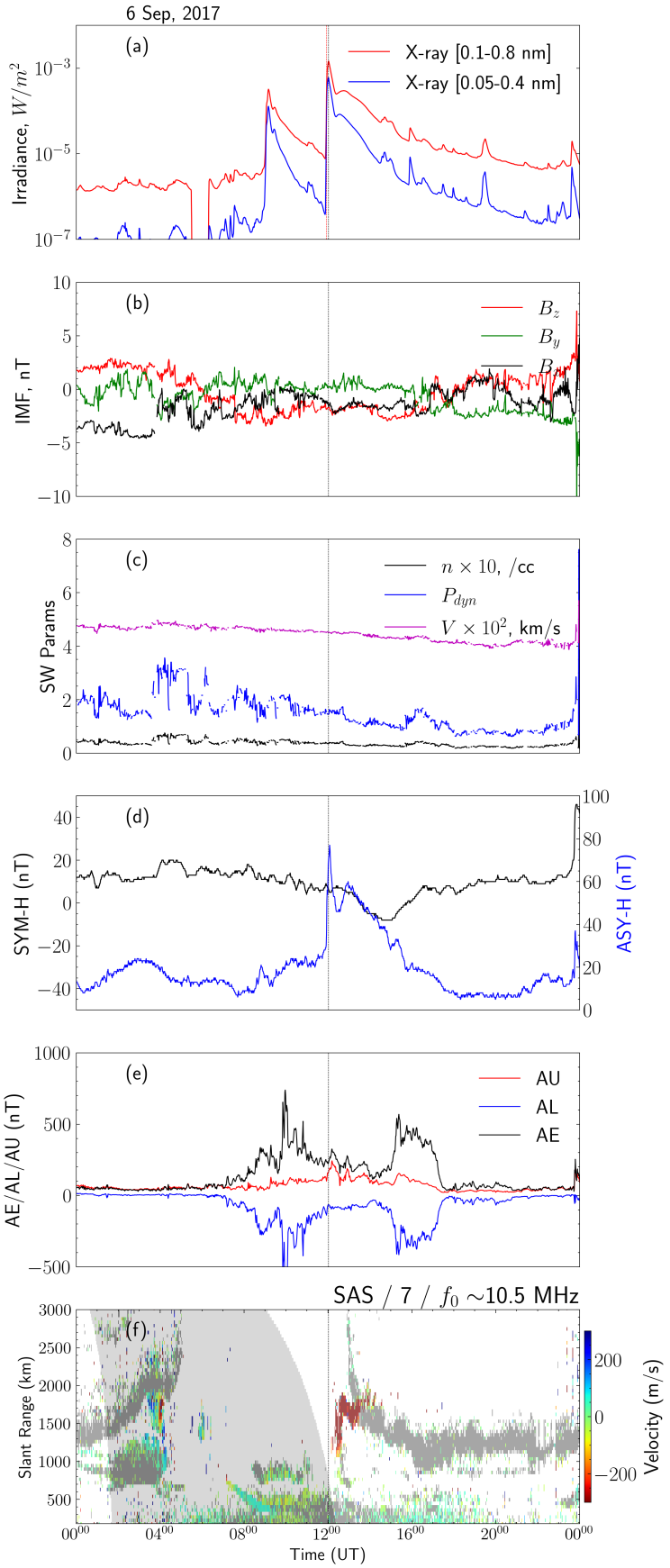

Figure 5. For the X9.3 class solar flare of 6th May 2017 the following parameters are shown: (a) solar irradiance from GOES-15 satellite, (b-c) IMF and solar wind [SW] conditions, (d) SYM-H (in black) and ASYM-H (in blue) indices, (e) auroral electrojets (AL [in blue], AE [in black], AU [in red]), and (f) a range-time intensity (RTI) plot displaying the Line of Sight Doppler velocity for beam 7. The vertical black line in all panels represents the peak of the X9.3 class solar flare.

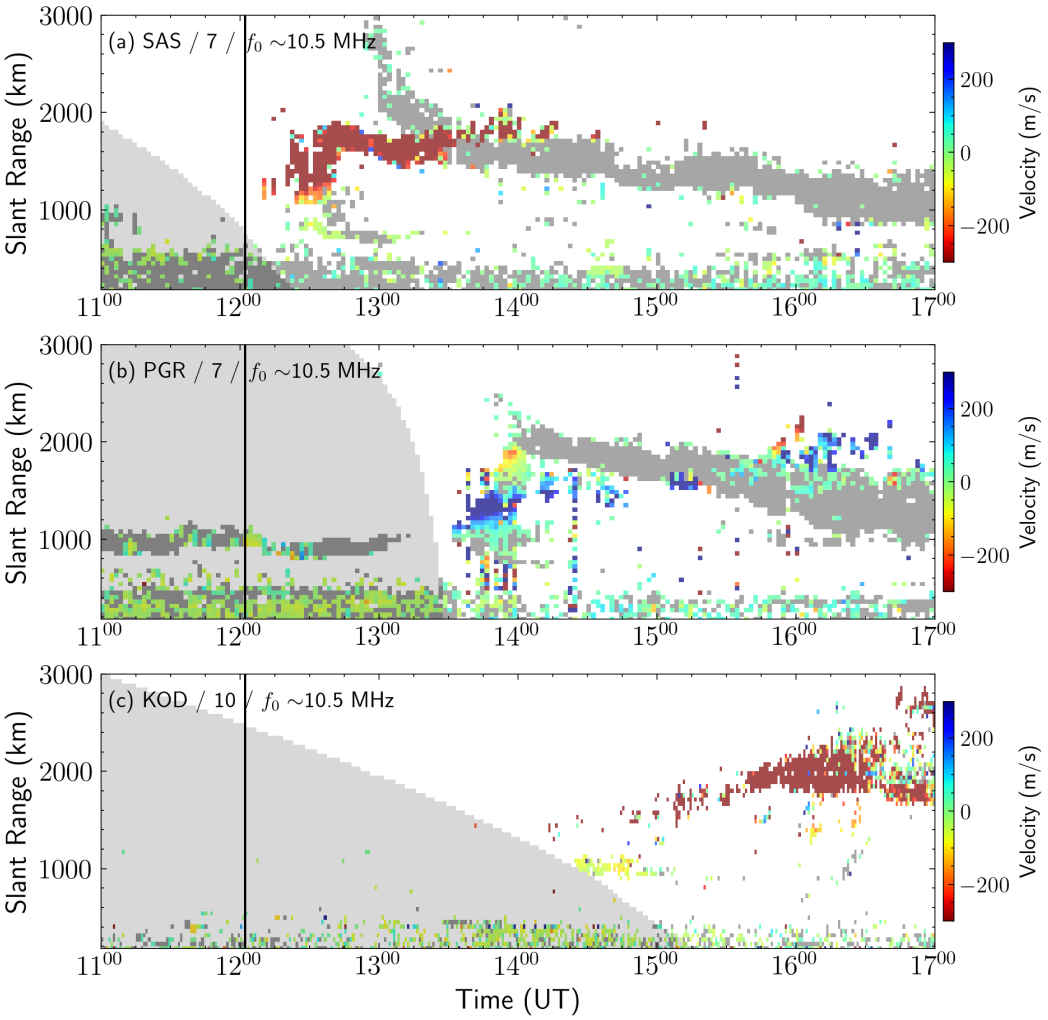

Figure 6. LoS Doppler velocity range-time intensity plot, observed by the SuperDARN high latitude radars situated across the Canadian sector (refer to Figure 2). The gray-shaded regions indicate nighttime at 300-km altitude over the Field of View of the corresponding radar beam. The vertical black line represents the peak of the X9.3 class solar flare at 12:02 UT.

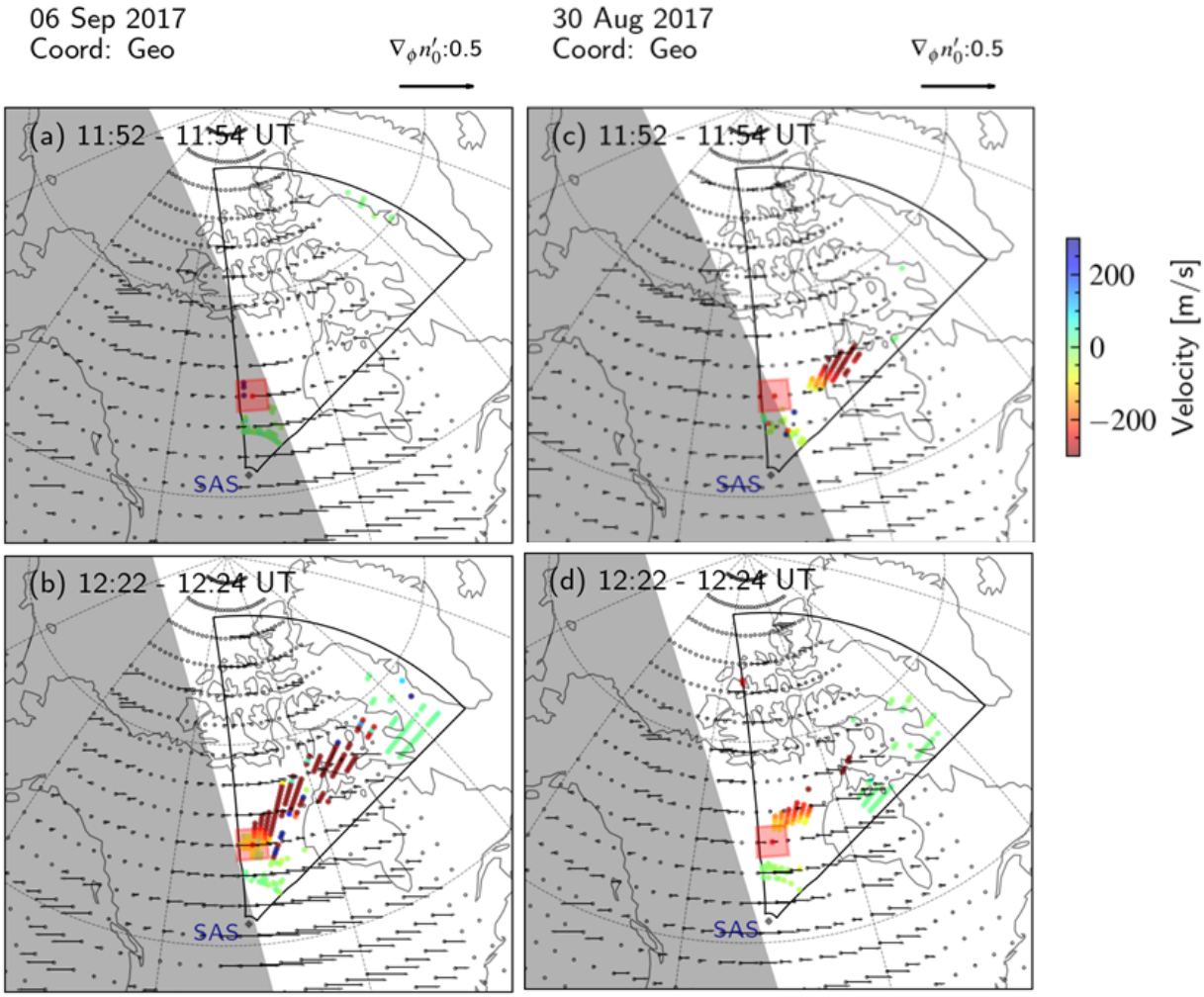

Figure 7. FoV plots of LoS Doppler velocity (color-coded by the color bar in panel (c)) recorded by the SuperDARN SAS radar overlaid with east-west TEC gradient (in black). The black arrows represent the TEC gradient along the longitude and have units in $TECu/^\circ$. The left (a-b) and right (c-d) columns present the observations during the X9.3 class flare on 6 September 2017 and the geomagnetic quiet day on 30 August 2017, respectively. The horizontal gradient of TEC is calculated in the $3^\circ \times 3^\circ$ grid cell shown in Figure 2.

to east. The ambient electric field, extending from the magnetosphere to the dawn side ionosphere, is directed equatorward (Ruohoniemi & Greenwald, 1996). The geometry near the dawn terminator, as shown in Figure 1, shows favorable conditions for GDI formation (Tsunoda, 1988). However, it is imperative to consider the magnitude of these physical parameters. Here we present evidence that the appearance of SuperDARN IS is primarily attributable to GDI, taking into account the plasma velocity and density gradient strengths.

In Section 2 we described how background parameters modulates the GDI via growth rate as shown in equation 1. Since we do not have measurements at individual point in space we need to adapt equation 1 to calculate a proxy for GDI growth rate. The GDI growth rate proxy is calculated using the east-west component of the SuperDARN LoS velocity ($V_0' = \frac{V_{los}}{cos\theta}$, where θ is the azimuth angle of the measured velocity vector) and TEC data (n_0'). The 'GDI growth rate proxy' given below, is deduced based on the first-order approximation of the GDI growth rate:

$$\gamma' = V_0' \times \frac{1}{n_0'} \frac{\partial n_0'}{\partial \phi} \tag{3}$$

Figure 8 offers a juxtaposition of GDI growth rate proxy values during the X9.3 solar flare on September 6, 2017 (depicted as black dots) and on a geomagnetically quiet day on August 30, 2017 (illustrated as red dots), for a high latitude ($\sim 60^\circ$). The top-to-bottom panels show TEC, TEC gradient with longitude (ϕ), i.e., $\frac{\partial n_0'}{\partial \phi}$, east-west component of the SuperDARN LoS Doppler velocity (V_0'), and growth rate proxy (γ'), respectively. The red vertical lines across all panels denote the solar flare peak at 12:02 UT. Notable findings are: (1) increase in n_0', $\frac{\partial n_0'}{\partial \phi}$, and V_0' on the flare day compared to quiet geomagnetic days, influencing γ', which is evident in the bottom panel; (2) significantly higher LoS Doppler velocity within the high latitude sector, resulting an $\approx$3-4 times higher γ' compared to the quiet day. By comparing panels (b) and (c) we see an approximately two-fold increase in zonal gradient of TEC, accompanied by a $\sim$10-fold increase in ion drift velocity as compared to the quiet day, suggesting an enhanced electric field at auroral latitudes in the dawn sector. As IS recorded by all the radars did not appear until the day-night terminator reach the FoV of the radars. Therefore, it is unlikely that the sources of the ionospheric scatter observed by the three radars are related to a substorm or other solar wind-driven phenomena. Drawing on empirical evidence presented in Figure 8 and work by Baker et al. (1986) and Hosokawa et al. (2000), we deduce that the abrupt irregularity appearance results from GDI triggered by flare-amplified plasma density gradients in the vicinity of the terminator. The polarizing electric field, induced by the charge separation due to the density gradient near the terminator, aligns with the background electric field, inducing Hall drift velocity along the background drift. In this context, the background plasma drift near the equatorward dawn terminator is characterized by Hall drift return flow of the ionospheric convection. Figure 7 shows that all radars detected LoS Doppler velocities, which are consistent with an eastward flow direction.

Using a SuperDARN polar-latitude radar (Inuvik) and a geospace coupled model LTR, Liu et al. (2021) showed a reduction in Cross Polar-Cap Potential (CPCP) and associated ionospheric convection flow velocity from radar following the same X9.3 flare on Sep 6, 2017. LTR model showed that the flare created an earthward displacement of the magnetopause. The study argues that the reduction in CPCP stem from a reconfiguration of magnetosphere convection and a decrease in the reconnection electric field. Their study showed that a sudden reduction in cross-polar electric field leads to a reduction in Joule heating, although flare enhanced ionospheric conductivity via sudden ionization. Our results suggest an increase in localized (near the dawn terminator) electric field indicated by the enhanced LoS velocity measurements from three SuperDARN auroral radars. This suggests a localized electric field enhancement. One possible source

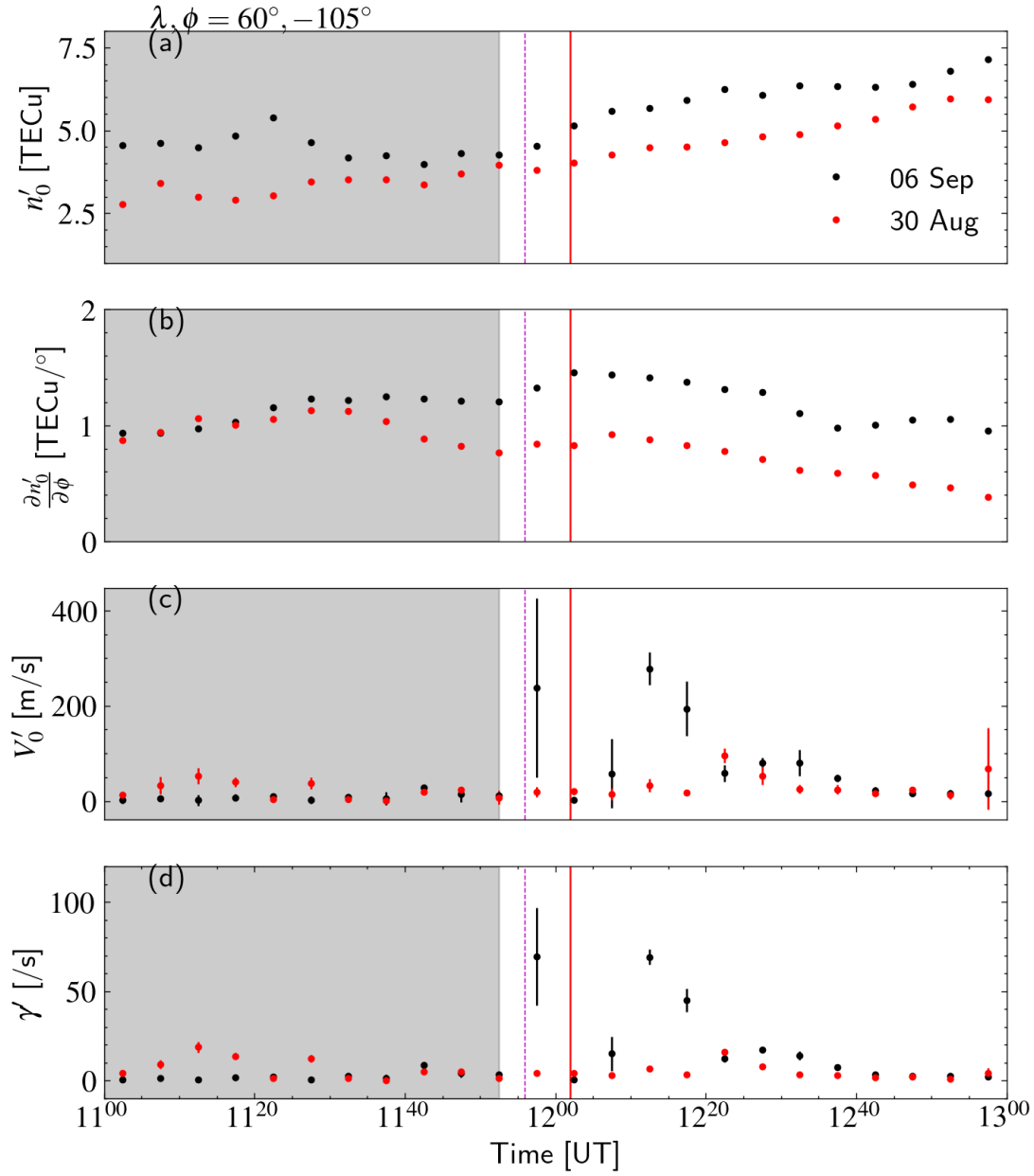

Figure 8. Comparison of four parameters, namely (a) Total Electron Content, (b) east-west horizontal gradient in TEC, (c) LoS Doppler velocity, and (d) proxy of the GDI growth rate, is performed for two specific dates: 6 September 2017 (shown in black) and 30 August 2017 (shown in red). The analysis focuses on a high latitude cell centered at geographic coordinates $(\lambda, \phi = 60°, -105°)$, which is indicated by the red shaded region mentioned in Figure 2 and represented by red circles in Figure 4(d). The cell's location is based on a $3° \times 3°$ latitude-longitude grid.

of this localized electric field enhancement can be the superposition of the polarization E-field that drives the GDI with the background ionospheric E-field. The background ionospheric E-field is imposed from the magnetosphere. The polarization E-field is generated from the separation of the charge along the dawn terminator. However, there are other mechanisms that may create localized intensification. While the cross-polar electric field is reduced due to a reduction in the efficiency of mechanical energy conversion in the dayside solar wind–magnetosphere, there can be pockets of localized enhanced electric field that drive high-velocity plasma flows. A comprehensive data-model study will be required to understand the sources of this localized E-field intensification.

Given our understanding that SuperDARN-observed IS is likely derived from flare-driven Gradient Drift Instability, the subsequent inquiry arises: What are the physical factors that could impact the mechanism driving GDI? Examining the geometry depicted in Figure 1 and equation 3, we ascertain that explicit parameters include the orientations of the background electric and magnetic fields with respect to the density gradient, the length scale of the density gradient, and the magnitude of the plasma flow velocity. To delve deeper into this analysis, we plan to undertake a subsequent modeling investigation.

5 Summary

In this investigation, we explored the impacts of an imposing X9.3-class flare, peaking at 12:02 UT on September 6, 2017, on the ionosphere's dawn side, as observed by SuperDARN HF radars located at high and middle latitudes. Using the SuperDARN observations and GNSS TEC data, we reported the following:

1. *Features observed in SuperDARN:* A sudden emergence of ionospheric scatter (IS) near the day-night terminator at high latitudes following the X9.3 flare were observed. The LoS Doppler velocity direction of these irregularities concurs with the convection flow's orientation adjacent to the equatorward border of the dawn terminator. High latitude radar-recorded LoS Doppler velocities reach ~ 300 m/s, significantly surpassing levels observed during the geomagnetically quiet day.
2. *Features observed in TEC and growth rate proxy, γ':* We observed an increased absolute Total Electron Content (TEC) and east-west TEC gradient near the dawn terminator after the X9.3 flare, compared to quiet geomagnetic days. The intensified density gradient creates favorable conditions for the Gradient-Drift Instability (GDI), apparent in γ'. GDI's growth rate proxy surges 3-4 times at the high latitude sector, relative to geomagnetically quiet days.

This study is one of the few observational record presenting flare-induced GDI-generated field-aligned irregularities recorded by the high latitudes SuperDARN radars. We found sudden appearance of SuperDARN IS is likely to be attributed to field-aligned irregularities generated by GDI, resulting from the flare-amplified east-west plasma gradient at F-region altitudes. How flare-altered ionospheric properties like conductivity and electric fields effect irregularity formation remains unclear. A comprehensive study combining first-principles modeling with ISR/satellite data on electron density and electric fields is necessary. This will help us identify geophysical parameters modulating flare-driven GDI and sources of localized electric field enhancements seen by SuperDARN.

Open Research

All the data and Python code are uploaded into the Zenodo available for public use (Chakraborty, 2022). The analysis and visualization were completed with the help of free, open-source software tools such as matplotlib (Hunter, 2007), IPython (Perez & Granger, 2007), pandas (McKinney, 2010), pyDARN (Shi et al., 2022), and others (e.g.,

Millman & Aivazis, 2011). The code is published in the Zenodo repository (Chakraborty, 2022). The authors acknowledge the use of SuperDARN data. SuperDARN is a collection of radars funded by national scientific funding agencies of Australia, Canada, China, France, Italy, Japan, Norway, South Africa, United Kingdom and the United States of America. We thank all participants in the worldwide SuperDARN collaboration for the distribution of SuperDARN data via `http://vt.superdarn.org/`. We wish to acknowledge the use of the NOAA/GOES X-ray data (from `https://www.swpc.noaa.gov/products/goes-x-ray-flux`) for flare confirmation and analysis. The authors also acknowledge the use TEC dataset obtained from the MIT Madrigal Database (`http://millstonehill.haystack.mit.edu/`). Data for TEC processing is provided from the following organizations: UNAVCO, SOPAC, IGN (France), IGS, CDDIS, NGS, IBGE (Brazil), RAMSAC (Argentina), CORS (Panama), Arecibo Observatory, LISN, Topcon, CHAIN (Canada), CRS (Italy), SONEL, RENAG (New Zealand), GNSS Reference Networks, Finnish Meteorological Institute, and SWEPOS. IMF, solar wind parameters, and geomantic conditions observations were obtained from the OMNI website: `https://omniweb.gsfc.nasa.gov` (Papitashvili & King, 2020).

Acknowledgments

SC thanks the Japanese Society for Promotion of Science (ID: PE22027) and the ISEE International Joint Research program for funding this research. SC also thanks to the National Science Foundation (NSF) for support under grants AGS-2512183 and AGS-2452540. XS was supported by NSF under grants AGS-1935110 and AGS-2025570, and by NASA under grants 80NSSC21K1677 and 80NSSC21K1683. AJC acknowledges support from ONR Grant N00014-17-1-2186 and N00014-22-1-2284 GPS TEC data products and access through the Madrigal distributed data system are provided to the community (`http://www.openmadrigal.org`) by the Massachusetts Institute of Technology (MIT) under support from US National Science Foundation grant AGS-1952737. We acknowledge the use of SuperDARN data. SuperDARN is a network of radars funded by national scientific funding agencies of Australia, Canada, China, France, Italy, Japan, Norway, South Africa, the United Kingdom, and the United States of America.

References

Amaechi, P. O., Akala, A. O., Oyedokun, J. O., Simi, K. G., Aghogho, O., & Oyeyemi, E. O. (2021). Multi-instrument investigation of the impact of the space weather events of 6–10 september 2017. *Space Weather*, *19*(12), e2021SW002806. Retrieved from `https://agupubs.onlinelibrary.wiley.com/doi/abs/10.1029/2021SW002806` (e2021SW002806 2021SW002806) doi: https://doi.org/10.1029/2021SW002806

Baker, K. B., Greenwald, R. A., Walker, A. D. M., Bythrow, P. F., Zanetti, L. J., Potemra, T. A., ... Rino, C. L. (1986). A case study of plasma processes in the dayside cleft. *J. Geophys. Res*, *91*, 3130-3144.

Belcher, S. R. G., Clilverd, M. A., Rodger, C. J., Cook, S., Thomson, N. R., Brundell, J. B., & Raita, T. (2021). Solar flare x-ray impacts on long subionospheric vlf paths. *Space Weather*, *19*(11), e2021SW002820. Retrieved from `https://agupubs.onlinelibrary.wiley.com/doi/abs/10.1029/2021SW002820` (e2021SW002820 2021SW002820) doi: https://doi.org/10.1029/2021SW002820

Belehaki, A., Tsagouri, I., Altadill, D., Blanch, E., Borries, C., Buresova, D., ... Watermann, J. (2020, August). An overview of methodologies for real-time detection, characterisation and tracking of traveling ionospheric disturbances developed in the TechTIDE project. *Journal of Space Weather and Space Climate*, *10*, 42. doi: 10.1051/swsc/2020043

Chakraborty, S. (2022). *shibaji7/highlatitudesfe: Flare effects on high latitude elec-*

trodynamics (version v1). Zenodo. Retrieved from https://doi.org/10.5281/zenodo.7329317

Chakraborty, S., Baker, J. B. H., Ruohoniemi, J. M., Kunduri, B., Nishitani, N., & Shepherd, S. G. (2019). A study of superdarn response to co-occurring space weather phenomena. *Space Weather*, *17*(9), 1351-1363. Retrieved from https://doi.org/10.1029/2019SW002179

Chakraborty, S., Qian, L., Ruohoniemi, J. M., Baker, J. B. H., Mclnerney, J. M., & Nishitani, N. (2021). The role of flare-driven ionospheric electron density changes on the doppler flash observed by superdarn hf radars. *Journal of Geophysical Research: Space Physics*, *126*(8), e2021JA029300. Retrieved from https://agupubs.onlinelibrary.wiley.com/doi/abs/10.1029/2021JA029300 (e2021JA029300 2021JA029300) doi: https://doi.org/10.1029/2021JA029300

Chakraborty, S., Ruohoniemi, J. M., Baker, J. B. H., & Nishitani, N. (2018). Characterization of short-wave fadeout seen in daytime superdarn ground scatter observations. *Radio Science*, *53*(4), 472-484. Retrieved from https://doi.org/10.1002/2017RS006488

Chamberlin, P. C., Eparvier, F. G., Knoer, V., Leise, H., Pankratz, A., Snow, M., ... Woods, T. N. (2020). The flare irradiance spectral model-version 2 (fism2). *Space Weather*, *18*(12), e2020SW002588. Retrieved from https://agupubs.onlinelibrary.wiley.com/doi/abs/10.1029/2020SW002588 (e2020SW002588 10.1029/2020SW002588) doi: https://doi.org/10.1029/2020SW002588

Cheng, N., Song, S., & Xie, H. (2019). Investigation of solar flares impact on gps/bds/galileo broadcast ionospheric models. *Radio Science*, *54*(1), 91-103. Retrieved from https://agupubs.onlinelibrary.wiley.com/doi/abs/10.1029/2018RS006591 doi: https://doi.org/10.1029/2018RS006591

Chisham, G., Lester, M., Milan, S. E., Freeman, M. P., Bristow, W. A., Grocott, A., ... Walker, A. D. M. (2007). A Decade of the Super Dual Auroral Radar Network (superdarn): Scientific achievements, new techniques and future directions. *Surveys in Geophysics*, *28*, 33-109. Retrieved from https://doi.org/ doi: 10.1007/s10712-007-9017-8

Coster, A. J., Goncharenko, L., Zhang, S.-R., Erickson, P. J., Rideout, W., & Vierinen, J. (2017). Gnss observations of ionospheric variations during the 21 august 2017 solar eclipse. *Geophysical Research Letters*, *44*(24), 12,041-12,048. Retrieved from https://agupubs.onlinelibrary.wiley.com/doi/abs/10.1002/2017GL075774 doi: https://doi.org/10.1002/2017GL075774

Curto, J. J., Marsal, S., Blanch, E., & Altadill, D. (2018). Analysis of the solar flare effects of 6 september 2017 in the ionosphere and in the earth's magnetic field using spherical elementary current systems. *Space Weather*, *16*(11), 1709-1720. Retrieved from https://doi.org/10.1029/2018SW001927

David, M., & Sojka, J. J. (2019). *Madrigal gps-tec maps of the high-latitude northern hemisphere 2009-2017 [data set]*. Utah State University. Retrieved from https://doi.org/10.26078/A7G8-5M30

Dodson, H. W., & Hedeman, E. R. (1958). Crochet-associated flares. *J. Astrophys*, *128*, 636-645.

Fejer, B. G., & Kelley, M. C. (1980). Ionospheric irregularities. *Reviews of Geophysics*, *18*(2), 401-454. Retrieved from https://agupubs.onlinelibrary.wiley.com/doi/abs/10.1029/RG018i002p00401 doi: https://doi.org/10.1029/RG018i002p00401

Frissell, N. A., Vega, J. S., Markowitz, E., Gerrard, A. J., Engelke, W. D., Erickson, P. J., ... Bortnik, J. (2019). High-frequency communications response to solar activity in september 2017 as observed by amateur radio networks. *Space Weather*, *17*(1), 118-132. Retrieved from https://agupubs.onlinelibrary.wiley.com/doi/abs/10.1029/2018SW002008 doi:

https://doi.org/10.1029/2018SW002008

Greenwald, R. A., Baker, K. B., Hutchins, R. A., & Hanuise, C. (1985). An HF Phased-Array Radar for Studying small-scale Structure in the High-Latitude Ionosphere. *Radio Science*, *20*, 63–79. Retrieved from https://doi.org/10.1029/RS020i001p00063

Hosokawa, K., Iyemori, T., Yukimatu, A. S., & Sato, N. (2000). Characteristics of solar flare effect in the high-latitude ionosphere as observed by the superdarn radars. *Adv. Polar Upper Atmos. Res.,*, *14*, 66-75. Retrieved from https://nipr.repo.nii.ac.jp/?action=repository_action_common_download&item_id=6304&item_no=1&attribute_id=18&file_no=1

Hosokawa, K., & Nishitani, N. (2010). Plasma irregularities in the dusk-side subauroral ionosphere as observed with midlatitude superdarn radar in hokkaido, japan. *Radio Science*, *45*(4). Retrieved from https://agupubs.onlinelibrary.wiley.com/doi/abs/10.1029/2009RS004244 doi: https://doi.org/10.1029/2009RS004244

Huang, Y., Richmond, A. D., Deng, Y., Chamberlin, P. C., Qian, L., Solomon, S. C., ... Xiao, Z. (2014). Wavelength dependence of solar irradiance enhancement during x-class flares and its influence on the upper atmosphere. *Journal of Atmospheric and Solar-Terrestrial Physics*, *115-116*, 87-94. Retrieved from https://www.sciencedirect.com/science/article/pii/S1364682613002824 (Sun-Earth System Exploration: Moderate and Extreme Disturbances) doi: https://doi.org/10.1016/j.jastp.2013.10.011

Hunter, J. D. (2007). Matplotlib: A 2d graphics environment. *Computing in Science & Engineering*, *9*(3), 90-95. doi: 10.1109/MCSE.2007.55

Jakowski, N., & Hoque, M. M. (2019). Estimation of spatial gradients and temporal variations of the total electron content using ground-based gnss measurements. *Space Weather*, *17*(2), 339-356. Retrieved from https://agupubs.onlinelibrary.wiley.com/doi/abs/10.1029/2018SW002119 doi: https://doi.org/10.1029/2018SW002119

Kelley, M. (2009). *The earth's ionosphere: Plasma physics and electrodynamics*. Academic Press. Retrieved from https://books.google.com/books?id=3GlWQnjBQNgC

Keskinen, M. J., & Ossakow, S. L. (1983). Theories of high-latitude ionospheric irregularities: A review. *Radio Science*, *18*(06), 1077-1091. doi: 10.1029/RS018i006p01077

Klimenko, M. V., Zakharenkova, I. E., Klimenko, V. V., Lukianova, R. Y., & Cherniak, I. V. (2019). Simulation and observations of the polar tongue of ionization at different heights during the 2015 st. patrick's day storms. *Space Weather*, *17*(7), 1073-1089. Retrieved from https://agupubs.onlinelibrary.wiley.com/doi/abs/10.1029/2018SW002143 doi: https://doi.org/10.1029/2018SW002143

Liu, J., Wang, W., Qian, L., Lotko, W., Burns, A. G., Pham, K., ... Wilder, F. (2021). Solar flare effects in the earth's magnetosphere. *Nature Physics*, *2021*(17), 17-7. Retrieved from https://doi.org/10.1038/s41567-021-01203-5

Manju, G., & Viswanathan, K. S. (2005). Response of the equatorial electrojet to solar flare related x-ray flux enhancements. *Earth Planets Space*, *57*, 3. Retrieved from https://doi.org/10.1186/bf03351819

McKinney, W. (2010). Data structures for statistical computing in python. In (p. 56–61). Proceedings of the 9th Python in science conference. doi: 10.25080/Majora-92bf1922-012

Millman, K. J., & Aivazis, M. (2011). Python for scientists and engineers. *Computing in Science & Engineering*, *13*, 2. doi: 10.1109/MCSE.2011.36

Nishimura, Y., Mrak, S., Semeter, J. L., Coster, A. J., Jayachandran, P. T., Groves, K. M., ... Ruohoniemi, J. M. (2021). Evolution of mid-latitude density

irregularities and scintillation in north america during the 7–8 september 2017 storm. *Journal of Geophysical Research: Space Physics*, *126*(6), e2021JA029192. Retrieved from https://agupubs.onlinelibrary.wiley.com/doi/abs/10.1029/2021JA029192 (e2021JA029192 2021JA029192) doi: https://doi.org/10.1029/2021JA029192

Nishioka, M., Saito, S., Tao, C., Shiota, D., Tsugawa, T., & Ishii, M. (2021, Feb 15). Statistical analysis of ionospheric total electron content (tec): long-term estimation of extreme tec in japan. *Earth, Planets and Space*, *73*(1), 52. Retrieved from https://doi.org/10.1186/s40623-021-01374-8 doi: 10.1186/s40623-021-01374-8

Nishitani, N., Ruohoniemi, J. M., Lester, M., Baker, J. B. H., Koustov, A. V., Shepherd, S. G., ... Kikuchi, T. (2019). Review of the accomplishments of mid-latitude super dual auroral radar network (superdarn) hf radars. *Progress in Earth and Planetary Science*, *6*(1), 27. Retrieved from https://doi.org/10.1186/s40645-019-0270-5

Papitashvili, N. E., & King, J. H. (2020). Omni 1-min data [data set]. *NASA Space Physics Data Facility*. (Accessed on (June 2024)) doi: 10.48322/45bb-8792

Perez, F., & Granger, B. E. (2007). Ipython: A system for interactive scientific computing. *Computing in Science & Engineering*, *9*, 3. doi: 10.1109/MCSE.2007.53

Qian, L., Burns, A. G., Chamberlin, P. C., & Solomon, S. C. (2010). Flare location on the solar disk: Modeling the thermosphere and ionosphere response. *Journal of Geophysical Research: Space Physics*, *115*(A9). Retrieved from https://agupubs.onlinelibrary.wiley.com/doi/abs/10.1029/2009JA015225 doi: https://doi.org/10.1029/2009JA015225

Ruohoniemi, J. M., & Greenwald, R. A. (1996). Statistical patterns of high-latitude convection obtained from goose bay hf radar observations. *J. Geoptiys. Res*, *101*, 21743-21763.

Ruohoniemi, J. M., Greenwald, R. A., Villain, J. P., Baker, K. B., Newell, P. T., & Meng, C.-I. (1988). Coherent hf radar backscatter from small-scale irregularities in the dusk sector of the subauroral ionosphere. *Journal of Geophysical Research: Space Physics*, *93*(A11), 12871-12882. Retrieved from https://agupubs.onlinelibrary.wiley.com/doi/abs/10.1029/JA093iA11p12871 doi: https://doi.org/10.1029/JA093iA11p12871

Sergeyev, V. (1977). Magnetic effect of chromospheric flares and electric field in the high-latitude ionosphere i, polar cap region. *Geomagnetizm i Aeronomiya - Geomagn. Aeron*, *17*, 291–297.

Shi, X., Schmidt, M., Martin, C. J., Billett, D. D., Bland, E., Tholley, F. H., ... McWilliams, K. (2022). pydarn: A python software for visualizing superdarn radar data. *Frontiers in Astronomy and Space Sciences*, *9*. Retrieved from https://www.frontiersin.org/articles/10.3389/fspas.2022.1022690 doi: 10.3389/fspas.2022.1022690

Tsunoda, R. T. (1988). High-latitude f region irregularities: A review and synthesis. *Rev. Geophys.*, *9*(3), 719-760. doi: 10.1109/MCSE.2007.55

Watanabe, D., & Nishitani, N. (2013). Study of Ionospheric Disturbances During Solar Flare Events Using the Superdarn Hokkaido Radar. *Advances in Polar Science*, *24*, 1. Retrieved from https://doi.org/10.3724/SP.J.1085.2013.00012

Yamauchi, M., Johnsen, M. G., Enell, C. F., Tjulin, A., Willer, A., & Sormakov, D. A. (2020). High-latitude crochet: Solar-flare-induced magnetic disturbance independent from low-latitude crochet. *Annales Geophysicae*, *38*, 6. Retrieved from https://doi.org/10.5194/ANGEO-38-1159-2020

Yamazaki, Y., & Maute, A. (2017, Mar 01). Sq and eej—a review on the daily variation of the geomagnetic field caused by ionospheric dynamo currents. *Space Science Reviews*, *206*(1), 299-405. Retrieved from https://doi.org/10.1007/

656 s11214-016-0282-z doi: 10.1007/s11214-016-0282-z